Article

Quintuple Function Integration in Two-Dimensional Cr(II) Five-Membered Heterocyclic Metal Organic Frameworks via Tuning Ligand Spin and Lattice Symmetry

Xiangyang Li,[¶] Qing-Bo Liu,[¶] Yongsen Tang,[¶] Wei Li, Ning Ding, Zhao Liu, Hua-Hua Fu, Shuai Dong, Xingxing Li,* and Jinlong Yang*

ACCESS | Metrics & More | Article Recommendations | Supporting Information

ABSTRACT: Two-dimensional (2D) semiconductors (SCs) integrated with two or more functions are the cornerstone for constructing multifunctional nanodevices but remain largely limited. Here, by tuning the spin state of organic linkers and the symmetry/topology of crystal lattices, we predict a class of unprecedented multifunctional SCs in 2D Cr(II) five-membered heterocyclic metal organic frameworks that simultaneously possess auxetic effect, room-temperature ferrimagnetism, chiral ferroelectricity (FE), electrically reversible spin polarization, and topological nodal lines/points. Taking 2D $Cr(TDZ)_2$ (TDZ = 1.2.5-thiadiazole) as an exemplification, the auxetic effect is produced by the antitetra-chiral lattice structure. The high temperature ferrimagnetism originates from the strong d-p direct magnetic exchange interaction between Cr cations and TDZ doublet radical anions. Meanwhile, the clockwise–counterclockwise alignment of TDZ's dipoles results in unique 2D chiral FE with atomic-scale vortex–antivortex states. 2D $Cr(TDZ)_2$ is an intrinsic bipolar magnetic SC where half-metallic conduction with switchable spin-polarization direction can be induced by applying a gate voltage. In addition, the symmetry of the little group C_4 of the lattice structure endows 2D $Cr(TDZ)_2$ with topological nodal lines and a quadratic nodal point in the Brillouin zone near the Fermi level.
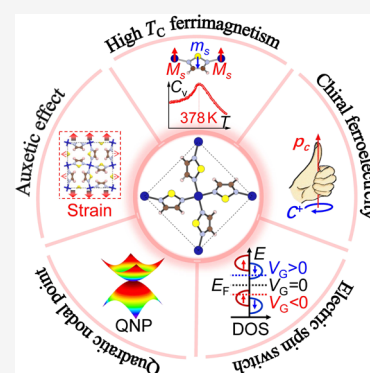
INTRODUCTION

Two-dimensional (2D) multifunctional materials with unique atomic-scale configurations and exotic electronic properties have aroused great interest in recent decades.[1,2] However, up to now, only limited numbers of such materials have been reported experimentally or theoretically, such as NiI_2,[3] $ReWCl_6$,[4] h-$Ti_2(O_2)_3$,[5] and AlB_6.[6] In addition, most are concentrated in traditional inorganic compounds with only two or three functions (Table S1). Developing 2D multifunctional materials with more functions and exotic properties remains a pending task.

Considering the structural rigidity and limited tunability of inorganic compounds, we turn our attention to organometallic materials with structural variability and rich functionalization possibilities.[7,8] Organometallic frameworks are hybrid porous materials composed of abundant metal nodes and inexpensive organic linkers.[8] By tuning metal nodes or organic linkers or the connectivity between them, they can possess functional properties with potential applications in traditional fields of gas separation, sensing, and optoelectronics[7−9] or emerging fields of electromechanical, magnetoelectronic, and topological quantum technologies.[10−16] For instance, by selecting benzimidazole as an organic linker, ultrathin poly-[Zn_2(benzimidazole)$_4$] sheets exhibit excellent performance in H_2/CO_2 gas separation.[17] By using dicyanoquinonediimine as a rotatory unit, the Cr(dicyanoquinonediimine)$_2$ sheet has

been predicted to be an auxetic magnet.[10] By changing the spin state of organic linkers from singlet to doublet and introducing a strong d-p direct ferrimagnetic (FiM) exchange interaction, high Curie temperature (T_C) magnetic semiconductors (SCs) Cr(pentalene)$_2$ (T_C = 560 K),[11] Cr(diketopyrrolopyrrole)$_2$ (T_C = 316 K),[15] and Cr(pyrazine)$_2$ (T_C = 342 K)[12,13] have been designed theoretically. Via distorting the out-of-plane K^+ counterions, ferroelectric 2D magnetic $K_3M_2[PcMO_8]$ (M = Cr-Co) sheets have been forecasted.[14] Through forming a Kagome lattice on a superconducting substrate, the experimentally synthesized 2D Cu_2(dicyanoanthracene)$_3$ sheet has been calculated and found to possess topological Dirac cones coupled with the substrate's superconductivity.[18]

Among numerous organometallic frameworks, a transition metal Cr atom as a common metal node has been widely used,[10−16] and its related planar tetracoordinate molecules or crystals have been extensively synthesized.[19−21] Although divalent Cr compounds are uncommon in chemistry, Perlepe
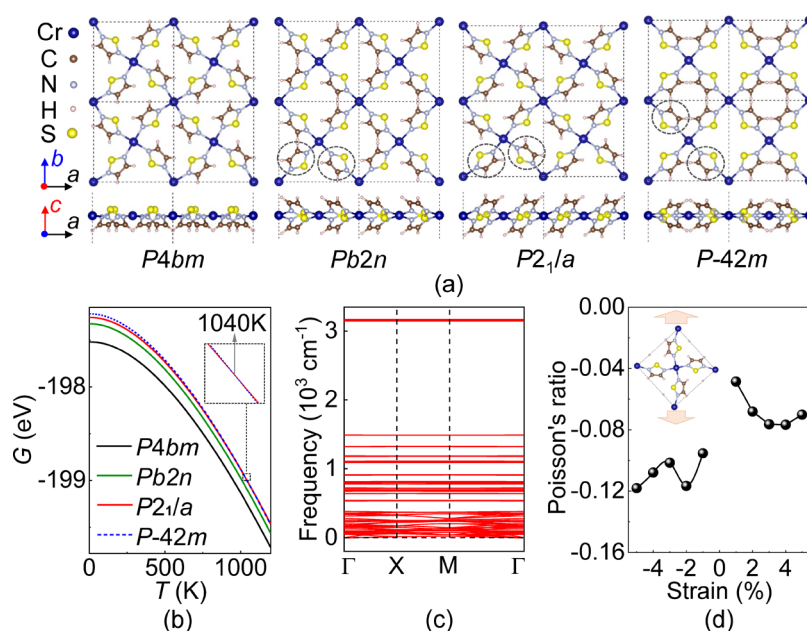
Figure 1. Structural and mechanical properties. (a) Geometrical structures of the four phases of $Cr(TDZ)_2$ (TDZ = 1.2.5-thiadiazole). (b) Gibbs free energies per unit cell of the four phases of $Cr(TDZ)_2$ as a function of temperature. The zoom-in inset marks the temperature of the phase transition point of P-$42m$ to $P2_1/a$. (c) Phonon spectrum of the most stable $P4bm$ phase. (d) Poisson's ratio of the $P4bm$ structure over a ±5% strain range along the diagonal direction.

et al. have prepared a layered $Li_{0.7}[Cr(pyrazine)_2]Cl_{0.7}\cdot$ 0.25(THF) (THF = tetrahydrofuran) crystal with room-temperature ferrimagnetism under a dinitrogen or argon atmosphere in which each Cr(II) is coordinated to four pyrazine organic linkers within the layers forming a square planar lattice.[21] If the pyrazine rings are replaced by inversion symmetry-breaking organic linkers, the functional properties can be further enriched as extra tunable degrees of freedom are introduced into the crystal structure.

In this work, by employing Cr(II) as a node and inversion symmetry-breaking five-membered aromatic heterocycles [TDZ, 1,2,5-oxadiazole (ODZ), 1,2,5-selenadiazole (SDZ)] as organic linkers, a class of unprecedented 2D SCs with up to five important functions, i.e., auxetic effect, room-temperature ferrimagnetism, chiral ferroelectricity (FE), electrical field controlled spin polarization, and topological nodal lines/ points, are predicted in metal organic frameworks (MOFs) with a square planar coordination structure. As exemplified by the $Cr(TDZ)_2$ sheet, due to the anti-tetra-chiral square lattice, auxetic effect emerges along the diagonal direction with a negative Poisson's ratio (NPR) of about −0.12. At the same time, the strong d-p direct magnetic exchange interaction between Cr cations and TDZ doublet radicals enables room-temperature ferrimagnetism with T_C = 378 K. Moreover, 2D chiral FE with atomic-scale vortex−antivortex states is discovered as a result of the coexistence of clockwise− counterclockwise dipoles, which have previously been shown to exist only in extremely rare cases and complex heterojunctions.[22,23] The electronic band structure indicates that 2D $Cr(TDZ)_2$ not only belongs to a special class of bipolar magnetic SCs (BMSs)[24,25] with the carriers' spin orientation readily reversible by electrical gating but also is a topological material with square nodal lines (SNLs) and a quadratic nodal point (QNP) protected by the C_4 crystal symmetry in the first Brillouin zone near the Fermi level. For practical applications, these multifunctional materials provide

an excellent platform to study the proximity effect between different properties. Moreover, by combining different functions, some high-performance spintronic devices can be designed, such as ultrahigh-density data storage devices.

RESULTS AND DISCUSSION

Possible Structures of the $Cr(TDZ)_2$ Sheet. Due to the lack of inversion symmetry, each five-membered aromatic heterocyclic structure has two different orientations with respect to the lattice plane, leading to the diversification of crystal structures formed with Cr atoms. Taking the TDZ organic ring as an example, Figure 1a shows four low energy structures of the $Cr(TDZ)_2$ sheet with point groups of $P4bm$, $Pb2n$, $P2_1/a$, and P-$42m$ symmetry, respectively. In these structures, four TDZ organic rings form an approximately square planar coordination with the Cr atoms, and each TDZ unit is connected by two adjacent Cr atoms. The four organic rings are arranged clockwise or counterclockwise around Cr atoms, with the ring planes presenting an inclination angle of about 43° with respect to the ab lattice plane. The unit cell parameters are $a = b$ = 9.14 Å for the $P4bm$ phase, $a = b$ = 9.12 Å for the $Pb2n$ phase, a (b) = 9.20 (8.66) Å for the $P2_1/a$ phase, and $a = b$ = 9.24 Å for the P-$42m$ phase. For the $P4bm$ structure, the S atoms in TDZ rings are all on one side of the ab plane. The panel on the left side of Figure 1a shows one possible structure in which all S atoms are located on the upper side of the lattice plane. Such spatial inversion symmetry-breaking gives rise to the electric polarization and FE of the structure (to be elaborated later). In contrast, when the S atoms in two ortho or para TDZ rings are on the other side of lattice plane [see the rings enclosed by dotted circles in other panels of Figure 1a], the corresponding $Pb2n$, $P2_1/a$, and P-$42m$ structures are formed and tend to be antiferroelectric.

First-principles calculations identify that the Gibbs free energy of the $P4bm$ crystal at 0 K is 0.19, 0.26, and 0.30 eV per unit cell lower than those of $Pb2n$, $P2_1/a$, and P-$42m$ crystals,
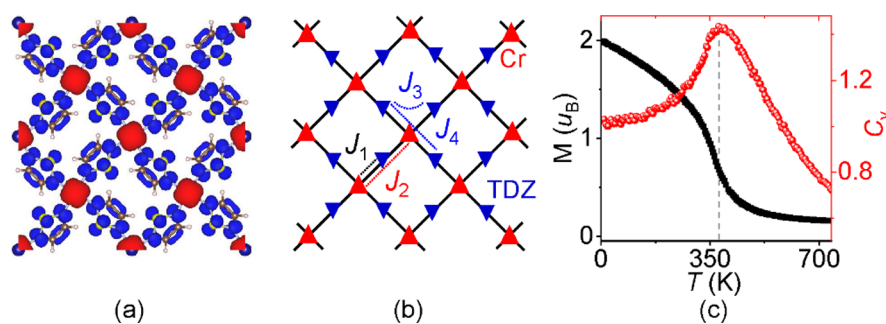
Figure 2. Room-temperature ferrimagnetism. (a) Spin density distribution of the $Cr(TDZ)_2$ sheet with a $P4bm$ symmetry in the ground FiM state. Red and blue indicate up and down spins, respectively. (b) Nearest neighbor and next-nearest neighbor spin exchange paths for the $Cr(TDZ)_2$ sheet. The exchange-coupling parameters J_k ($k = 1\sim4$) are also marked. J_1 represents the interaction between the Cr atom and nearest neighbor TDZ. J_2 means the interaction between the nearest two Cr atoms. J_3 and J_4 serve as the interaction between the nearest and next-nearest two TDZ. (c) Magnetic moment (M) per chemical formula (black) and specific heat C_v (red) as a function of temperature by using a Monte Carlo simulation based on the classic Heisenberg model. The magnetic exchange parameters used here are calculated with the HSE06 functional.

respectively. As the temperature increases, the $P4bm$ structure remains to possess the lowest energy (Figure 1b), implying it is the ground state configuration. For the $P2_1/a$ and $P\text{-}42m$ crystals, a phase transition is observed at about 1040 K; see the inset of Figure 1b. Moreover, we have also considered other two possible crystals with different space groups (Table S2), all of which have higher energies than the $P4bm$ phase, and thus we mainly focus on the most stable $P4bm$ phase in the following studies.

Dynamic and Thermal Stability Analysis. As shown in Figure 1c, no obvious imaginary frequency is observed from the calculated phonon spectrum, indicating that the $Cr(TDZ)_2$ sheet is dynamically stable. Although some extremely small imaginary frequencies (less than 1.8 cm^{-1}) exist near the Γ point by using a $3 \times 3 \times 1$ supercell (Figure S1), they are considered to be not physical and caused by size and boundary effects,[26] which are expected to disappear in a relatively large supercell; see Figures S2 and S3 for the detailed tests. Due to the rather large lattice constant, the phonon bands are dispersionless. The existence of a large number of soft phonon modes illustrates the flexibility of the $Cr(TDZ)_2$ sheet.[11] For example, the maximum Young's modulus of the $P4bm$ structure is only 39 GPa (Figure S4), which is much smaller than that of MoS_2 (170−370 GPa).[27] Besides the dynamic stability, the thermal stability is further examined by performing ab initio molecular dynamic (AIMD) simulation at 400 K (Figure S1). It is found that during the simulation, the total energy always fluctuates near its equilibrium value without a sudden drop, and the lattice structure can maintain well without any reconstruction after 9 ps, confirming that the structure is thermally stable.

Auxetic Effect. Interestingly, the structure of the $Cr(TDZ)_2$ sheet belongs to the so-called anti-tetra-chiral lattice capable of exhibiting auxeticity,[28] therefore a distinct auxetic effect and NPR along the diagonal direction are expected (see Figure 1d). Here, the Poisson's ratio is defined as $-\partial\varepsilon_t/\partial\varepsilon_a$, where ε_t and ε_a are strains in the transverse and corresponding longitudinal directions, respectively.[29] The maximum value of NPR can reach about -0.12 in the 5% strain range. This value is smaller than that of 2D $Cr(dicyanoquinonediimine)_2$ (-0.85),[10] but comparable to most reported 2D inorganic auxetic materials, such as Ag_2S (-0.12),[30] Be_5C_2 (-0.16),[31] and SnSe (-0.17).[32] The auxetic property endows 2D $Cr(TDZ)_2$ with potential applications in nanomechanics[33] (such as auxetic strain-sensors and auxetic pumps) and defense

and aerospace aspects. In addition, it can be seen from the Poisson's ratio curve of 2D $Cr(TDZ)_2$ as a function of in-plane angle θ (Figure S4) that the mechanical property is anisotropic.

Room-Temperature Ferrimagnetism. In the $Cr(TDZ)_2$ sheet, each TDZ ring grabs about 0.78e from adjacent Cr atoms based on Bader charge analysis, resulting in the formation of TDZ doublet radical anions and Cr(II) cations. For the Cr(II) cation, the five d orbitals are split into four groups: (d_{xz}, d_{yz}), d_{z^2}, d_{xy}, and $d_{x^2-y^2}$ in a square planar ligand field (Figure S5 and Note S1). The $d_{x^2-y^2}$ orbital's contribution to the spin moment is minor due to the relatively small difference in electron occupancy numbers between the spin-up and spin-down energy levels. The spin moment of Cr(II) originates mainly from the spin-up energy level of the other four d orbitals with an electronic configuration of $d_{xz}^{0.92} d_{yz}^{0.92} d_{z^2}^{0.89} d_{xy}^{0.85} d_{x^2-y^2}^{0.61}$. Therefore, the magnetic moment of Cr(II) is estimated to be 3.4 μ_B with a spin of $S = 2$. For the TDZ radical anion, the three average p orbitals of S, C, and N atoms are split into two groups: (p_x, p_y), p_z (Figure S5 and Note S1). Compared with p_x and p_y orbitals, the p_z orbital contributes the most to the spin moment. Because the occupancy number of the spin-down energy level of all the p orbitals is larger than that of the spin-up energy level, the total magnetic moment of the TDZ radical anion is negative and approximately -0.6 μ_B with a spin of $S = 1/2$. According to the above analysis, we can deduce that the total magnetic moment of $Cr(TDZ)_2$ is approximately 2 μ_B per chemical formula.

To determine the magnetic ground state of the $Cr(TDZ)_2$ sheet, eight different magnetic states, including one ferromagnetic (FM) state, two anti-FM (AFM) states, and five FiM states (Figure S6), are investigated. The results show that the FiM1 state is the magnetic ground state, where the spins on Cr(II) cations are all antiparallelly aligned with the spins on TDZ radicals. Figure 2a shows the spin density distribution of the FiM1 state. Obviously, the spin density on the TDZ radicals is mainly distributed over the p_z orbitals of all nonmetallic C, N, and S atoms. It is the strong d-p direct exchange interaction between the d-electron spins of Cr and p-electron spins of TDZ that makes the magnetic ground state of the system to be the FiM1 state with an energy of 0.85 eV per chemical formula lower than that of the FM state.

For practical spintronic applications, it is crucial to keep the magnetic ordering of the $Cr(TDZ)_2$ sheet above room temperature. To confirm this, we perform Monte Carlo
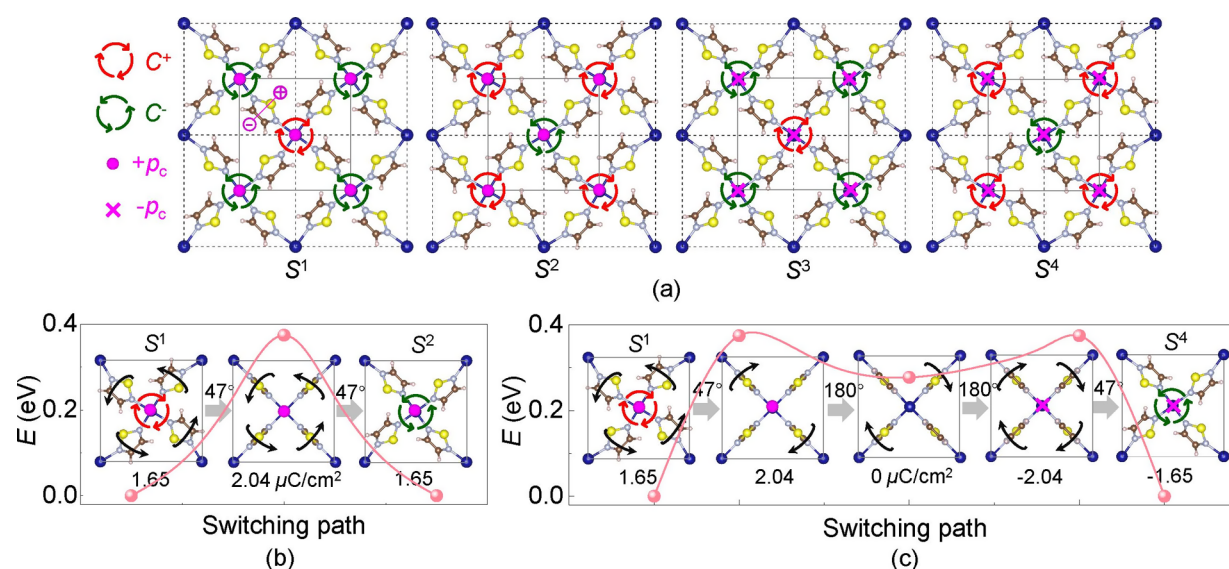
Figure 3. Chiral FE with atomic-scale vortex−antivortex states. (a) Four possible chiral vortex−antivortex states S^i (i = 1∼4) of the $Cr(TDZ)_2$ sheet with a $P4bm$ symmetry. C^+ represents a vortex state comprising four clockwise dipoles around the central Cr atoms, and C^- means an antivortex state comprising four counterclockwise dipoles around the central Cr atoms. $+p_c$ ($-p_c$) serves as a state of total electric polarization that is outward (inward) perpendicular to the ab lattice plane. (b) Possible path and energy barrier for the transition from S^1 to S^2. (c) Possible path and energy barrier for the transition from S^1 to S^4.

simulations based on the classical Heisenberg model Hamiltonian,[34]

$$H = -\sum_k \sum_{i>j} \sum_j J_k S_i \cdot S_j + \sum_i D_i S_{iz}^2 \quad (1)$$

where J_k is four different exchange-coupling parameters presented in Figure 2b and S_i is the spin of Cr or TDZ. D_i is magnetic anisotropy parameter. Since the TDZ radical is composed of light elements, its magnetic anisotropy energy (MAE) is relatively weak. Therefore, during the density functional theory (DFT) calculation, we assign the total MAE of 494.1 μeV per chemical formula to the Cr atoms (with a value of 123.5 μeV), and the MAE of TDZ radicals is simply taken as zero. The direction of magnetic easy axis of the $Cr(TDZ)_2$ sheet is perpendicular to the lattice plane. The values of J_k are deduced from the energy differences between the different magnetic states; see Note S2 and Table S3. Figure 2c shows the temperature-dependent spin magnetic moment (M) per chemical formula in which the M gradually decreases from 2 μ_B to 0 with the increase of temperature. The specific heat $C_v = (\langle E^2 \rangle - \langle E \rangle^2)/T^2$ is obtained after the system reaches equilibrium at a given temperature, and the peak position manifests that the FiM−paramagnetic transition occurs at the Curie temperature T_C of 378 K, significantly higher than room temperature.

Chiral FE. More intriguingly, due to the inversion symmetry-breaking feature of five membered heterocycles, the negative charge center of the TDZ ring does not coincide with the positive one, thus an intrinsic proper electric polarization would be present. Therefore, each TDZ ring can be regarded as an electric dipole, which is inclined from the c-axis at an angle of 47° and reversible in the dipole direction by rotating the TDZ rings. The superimposed c-axis component of all TDZ dipoles induces the ferroelectric polarization ($\pm p_c$) of the $Cr(TDZ)_2$ sheet along the c-direction. In the ab plane, four noncollinear electric dipoles connecting one of the Cr atoms form an atomic-scale vortex state C^+, and another four

electric dipoles linking the adjacent Cr atoms form an antivortex state C^- (Figure 3a). Such two states assemble a 2D lattice with chiral vortex−antivortex polar states down to the monolayer scale, which is distinct from the nanometer-scale chiral vortex−antivortex arrays in a complex hetero-junction structure with alternating lead titanate and strontium titanate layers.[23] The vortex and antivortex states that always appear in pairs result in complete cancellation of the electric polarization vectors in the ab plane (Figure S7), i.e., no macroscopic electric polarization.

Based on the above analysis, the noncollinear ferroelectric states of the $Cr(TDZ)_2$ sheet can be described by two ferroelectric order parameters $Q_1 = +C^+ + C^-$ in the ab plane and $Q_2 = +p_c + p_c$ along the c-direction, where Q_1 and Q_2 obviously have two degenerate modes $\pm Q_1$ and $\pm Q_2$, respectively. As shown in Figure 3a, those four order parameters can describe four degenerate ferroelectric vortex states: S^1 ($+Q_1, +Q_2$), S^2 ($-Q_1, +Q_2$), S^3 ($+Q_1, -Q_2$), S^4 ($-Q_1, -Q_2$). It is worth mentioning that the in-depth study of such ferroelectric materials with chiral vortex properties at the atomic scale is of great value for understanding the noncollinear ferroelectric and chiral ferroelectric physics.

By using the dipole correction scheme in DFT,[35] the calculated polarization values of the above four vortex states are all 1.65 μC/cm^2 (see Figure S8 for details), where the polarization directions of S^1 and S^2 are along the positive direction of the c-axis, while those of S^3 and S^4 are along the negative direction of the c-axis. Although the calculated polarization values are lower than those of ReWCl$_6$ (3.22 μC/cm^2)[4] and hexagonal YMnO$_3$ (5 μC/cm^2),[36] they are higher than those of bilayer BN (0.6 μC/cm^2),[37] bilayer SiC (0.25 μC/cm^2),[38] and Sc$_2$CO$_2$ (1.6 μC/cm^2).[39]

Figure 3b shows the transition path from S^1 to S^2. The four TDZ rings in the S^1 state first simultaneously rotate 47° counterclockwise to reach the transition state and then further rotate 47° counterclockwise to evolve to the S^2 state, where the energy barrier is 0.37 eV per TDZ. At the transition state, all

the TDZ rings are perpendicular to the *ab* lattice plane, where the electric polarization along the *c*-axis reaches the maximum value of 2.04 $\mu C/cm^2$ and the vortex state feature disappears. The transition from S^1 to S^4 is complicated, and the corresponding energy barrier is also 0.37 eV per TDZ. Figure 3c illustrates one possible path. First the four TDZ rings in the S^1 state rotate 47° counterclockwise, next the two TDZ rings at the para position rotate 180° clockwise, then the other two TDZ rings rotate 180° clockwise, and finally the four TDZ rings simultaneously rotate 47° clockwise to get to the S^4 state. Specifically, a series of possible intermediate states exist throughout the transition, but none of them is stable after examining their phonon spectra. For example, an intermediate state without polarization [see the middle panel in Figure 3c] possesses an energy of 0.27 eV higher than the ground structure, and its phonon spectrum presents a certain imaginary frequency; see Figure S9. In addition, Figure S10 displays another possible transition path, where the energy barrier remains to be 0.37 eV. The transition from S^1 to S^3 is similar to that from S^1 to S^4 (Figure S11). Overall, we can infer that the energy barriers from S^i to S^j are all around 0.37 eV, the value of which is higher than that of WO_2Cl_2 (0.22 eV),[40] but lower than those of $K_3Fe_2[PcFeO_8]$ (0.38 eV)[14] and CrI_3 (0.65 eV).[41]

Here, it should be noted that in the $Cr(TDZ)_2$ sheet, there is no significant magnetoelectric coupling because the generation mechanisms of magnetism and FE are quite different; that is, the magnetism arises from the direct FiM *d-p* exchange coupling between Cr and TDZ, while the ferroelectric polarization is generated by the electronegativity difference between S and N or C. Thus, this material belongs to a type-I multiferroic.[42]

Electrically Reversible Spin Polarization. To reveal the electronic properties of the $Cr(TDZ)_2$ sheet, the band structures and density of states are calculated by using the HSE06 functional, as shown in Figure 4a. Obviously, its valence band (VB) maximum and conduction band (CB) minimum are both at the Γ point, meaning it is a direct SC with a band gap of 1.60 eV. The VB and CB are 100% spin polarized in opposite spin channels, suggesting the $Cr(TDZ)_2$ sheet belongs to an intrinsic BMS.[24,25] According to the density of states distribution of each atom, we can infer that the VB and CB states are mainly contributed by the *p* orbitals of N, C, and S atoms on the TDZ rings. The electronic states near −2 eV below the VB are mainly contributed by the *d* orbitals of Cr atoms, and those near 2.6 eV above the CB are contributed not only by the *d* orbitals of Cr atoms but also by a small amount of *p* orbitals of S atoms. These characteristics are consistent with the shape of the spatial distribution of electronic states in Figure S12.

When a positive electric gate is applied, the electrons in $Cr(TDZ)_2$ will be extracted, resulting in a hole doping effect. It causes the Fermi level to move down to the VB [such as at a concentration of -1.2×10^{14} cm^{-2} in Figure 4b], and the carrier's spin polarization is fixed at the spin-down channel. Similarly, when a negative electric gate is used, the electrons will be injected into the $Cr(TDZ)_2$, inducing an upward shift of the Fermi level to the CB [such as at a concentration of $+1.2 \times 10^{14}$ cm^{-2} in Figure 4b], and the carrier's spin polarization is fixed at the spin-up channel. In short, the direction of carrier's spin polarization can be controlled by reversing the polarity of the electric gate.
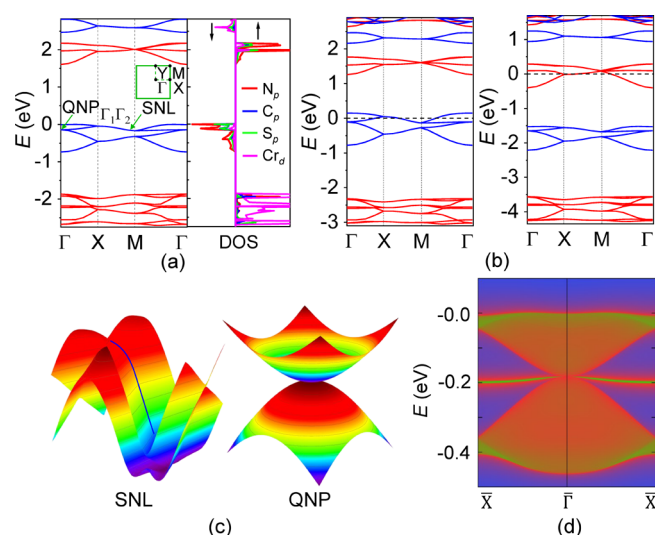

Figure 4. Electrically reversible spin polarization and topological nodal lines/points. (a) Spin-polarized band structures and projected density of states for the $Cr(TDZ)_2$ sheet with the HSE06 functional. Red and blue lines represent spin-up and spin-down bands, respectively. The inset shows high-symmetry points in the first Brillouin zone. SNL represents a nodal line with square characteristics, and QNP represents a nodal point with quadratic dispersion. (b) Band structure of the $Cr(TDZ)_2$ sheet for hole doping (left) and electron doping (right) with a carrier concentration of $\pm 1.2 \times 10^{14}$ cm^{-2}. Positive and negative values represent electron and hole doping, respectively. (c) Three-dimensional energy band structures of an SNL and a QNP near the Fermi level. (d) Dirac-cone edge states for QNP. Here, $\bar{X}$ points are the *X*'s projection of the two-dimensional Brillouin zone in the inset of (a) along the (010) surface Brillouin zone.

Topological Nodal Lines/Points. Moreover, the energy bands near the Fermi level possess doubly degenerate nodal lines on the *X-M* path protected by a 2D irreps $\Gamma_1\Gamma_2$ in little group C_4, and there exists a QNP[43] with a zero Chern number protected by a 2D irreps Γ_5 in point group C_{4v} at the Γ point (Note S3). The nodal lines are distributed at the boundary of the 2D Brillouin zone, showing a square-shaped feature; see the inset of Figure 4a. These topological properties are very important in physics, since they can induce the special Landau level,[44] negative magnetoresistance,[45,46] and quantized circular photogalvanic effect.[47,48] By investigating the distributions of projected density of states, one can derive that the states of SNLs[49] and QNP near the Fermi level are dominated by the *p* orbitals of N, C, and S atoms. For clarity, Figure 4c shows the 3D band characteristics of an SNL and a QNP near the Fermi level.

To further verify the topological properties, we calculate the edge states of the $Cr(TDZ)_2$ sheet along the (100) direction. As displayed in Figure 4d, the QNP at the $\bar{\Gamma}$ point forms a clear quadratic Dirac cone edge state, which proves that it is nontrivial. Since the SNLs are projected into the one-dimensional Brillouin zone, the corresponding edge states cannot be observed. In addition, after considering the spin-orbit coupling (SOC) effect, the QNP of $Cr(TDZ)_2$ opens a topological gap of 7 meV (Figure S13), which is comparable to those of $Mn(C_6H_5)_3$ (9.5 meV),[50] $Mn_2C_6S_{12}$ (7~15 meV),[51] and Cr_2Se_3 (6.7 meV).[52]

Similar Multifunctional SCs. Based on the example of the $Cr(TDZ)_2$ sheet, we can easily expand into a range of multifunctional organometallic SCs by substituting the TDZ

organic linkers with other five-membered heterocycles, such as $Cr(ODZ)_2$ and $Cr(SDZ)_2$. All structures are dynamically and thermally stable (Figures S1−S3). For the $Cr(ODZ)_2$ sheet, the ground state is the antiferroelectric $P2_1/a$ state. In contrast, the ground state of the $Cr(SDZ)_2$ sheet is ferroelectric with an electric polarization of about 1.01 $\mu C/cm^2$ (Table S4), slightly weaker than that of the $Cr(TDZ)_2$ sheet. The transition energy barriers between different ferroelectric phases remain around 0.37 eV. The auxetic effect of these two extended sheets is superior to that of the $Cr(TDZ)_2$ sheet, where the maximum absolute value of NPR reaches 0.17 and 0.13 for $Cr(ODZ)_2$ and $Cr(SDZ)_2$ sheets, respectively (Figure S14). Both T_C are above room temperature with the highest being 410 K (Figure S15 and Tables S5 and S6). Meanwhile, the $Cr(ODZ)_2$ and $Cr(SDZ)_2$ sheets are also BMSs with oppositely spin-polarized VB and CB edges (Figure S16). Compared with $Cr(TDZ)_2$, the QNP of $Cr(SDZ)_2$ opens a larger topological gap of 33 meV from the HSE + SOC band structure, providing a potential platform for studying the quantum anomalous Hall effect.

Proposed Experimental Synthesis and Characterization Methods. For the experimental fabrication of these 2D organometallic frameworks, one possible route is to adopt top-down technologies. Similar to the synthesized $Li_{0.7}[Cr(pyz)_2]Cl_{0.7} \cdot 0.25(THF)$ crystal,[21] their bulk layered crystals are first realized by combining redox-active coordination chemistry[53] and postsynthetic reduction modification,[21] and then the corresponding sheets are achieved through mechanical exfoliation. Another possible route is to use bottom-up methodologies. Metal atoms and organic linker molecules are deposited onto a metal surface by molecular beam evaporation or electron beam evaporation to induce their self-assembly to form 2D organometallic frameworks. Such preparation strategies have been widely used to synthesize similar coordination structures, e.g., Mn-$TCNQ_4$ network,[54] Ni-TPyP network,[55] TPA-Cs, BDA-Cs, and TDA-Cs networks.[56] In addition, the ratio of Cr to organic linkers needs to be well controlled in the experimental synthesis to ensure that all five functions, i.e., auxetic effect, room-temperature ferrimagnetism, chiral FE, electrical field controlled spin polarization, and topological nodal lines/points, are achieved simultaneously; see Note S4, Figure S17, and Table S7 for the detailed discussion of $Cr_n(TDZ)_m$.

As for the experimental characterization, the mechanical properties including Poisson's ratio can be elucidated by the Brillouin scattering experiment.[57,58] For the magnetic property, the magnetic critical temperature can be obtained by measuring the change of magnetic moment with the temperature using the MicroSense vibrating sample magnetometer.[21,59] For the FE, the ferroelectric phase transition temperature and the strength of ferroelectric polarization can be determined by testing the dielectric or ferroelectric loop of the sample.[60] For the electrically reversible spin polarization, it can be verified by applying a gate voltage with different directions on the sample and then measuring the carrier's spin-polarization direction by the spin-polarized tunneling experiment.[61,62] For the topological property, the inelastic neutron scattering experiment can be performed to observe the energy distribution in the momentum space, thereby verifying the existence of topological nodes and nodal lines.[63]

Potential Applications. In practical applications, integrating so many functional properties into a single sheet can offer two advantages. The first is to provide an ideal platform to

study different kinds of proximity effects.[64] Specifically, as shown in Figure 5a, the proximity effects between FiM, FE,
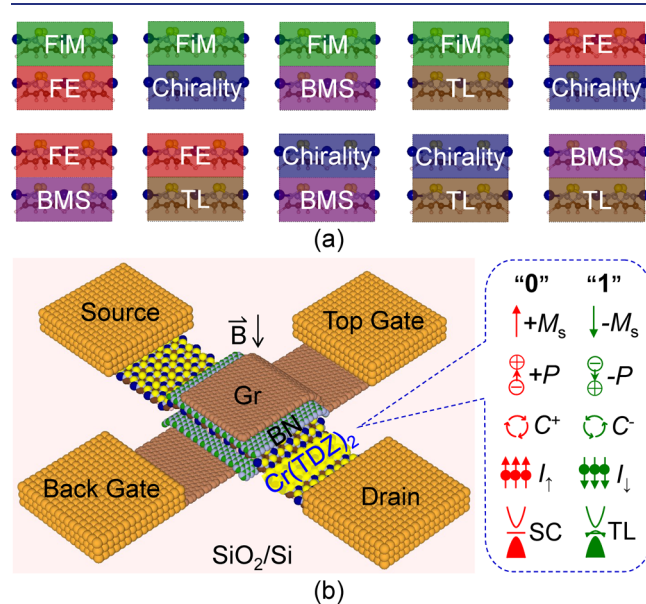

Figure 5. Schematics of applying multifunctional $Cr(TDZ)_2$ in studying proximity effects and designing ultrahigh-density data storage devices. (a) Constructing a $Cr(TDZ)_2$-based homojunction to explore the proximity effect among FiM, FE, chirality, BMS, and topology (TL). (b) 3D schematic diagram of a field-effect transistor device based on the $Cr(TDZ)_2$ sheet. The field-effect transistor is fabricated by sequentially vertically stacking graphene (Gr), BN, $Cr(TDZ)_2$, BN, and Gr sheets on a SiO_2/Si substrate. The top and back gates are connected to one of the Gr sheets, respectively. The source and drain electrodes are linked to the $Cr(TDZ)_2$ sheet. The inset on the right shows five pairs of possible storage parameters, that is, spin magnetic moment ($\pm M_s$), electric polarization ($\pm P$), chirality ($C^\pm$), spin polarized current ($I_{\uparrow/\downarrow}$), and SC/topological half-metal.

chirality, BMS, and TL can be investigated by constructing a bilayer homojunction. Such a homojunction can effectively avoid additional effects caused by lattice mismatch of the heterojunction. The second is to improve the performance of related spintronic devices through the synergy between multiple functions. For instance, when the five functional properties of FiM, FE, chirality, BMS, and TL are simultaneously applied to a data storage device, the storage density can be increased 16 (2^4) fold compared to a single-function device since each function contains two switchable states. The switching between different storage states can be realized under an external electric or magnetic field. Figure 5b displays a field effect transistor with the $Cr(TDZ)_2$ sheet as a channel material to illustrate the specific modulation method in different functions. The orientation of spin moment ($\pm M_s$) can be changed by applying a magnetic field $\vec{B}$ perpendicular to the sheet plane. The transition between different electrical polarization ($\pm P$) states and chiral ($C^\pm$) states can be achieved by assigning a certain electric field. Both the direction of current spin polarization ($I_{\uparrow/\downarrow}$) and the transition from trivial SC to topological half-metal including boundary states can be modulated by using different gate voltages.

Besides potential applications in proximity effect and high-density data storage devices, the proposed 2D Cr(II) five membered heterocyclic MOFs may also be useful in gas separation, optoelectronics, etc.[65] For example, in gas

separation, they have a similar pore size (2.7 Å) to ultrathin poly[Zn_2(benzimidazole)$_4$] sheets and thus may have a potential advantage for H_2/CO_2 separation.[17] In optoelectronics, since these MOFs are direct SCs with bandgaps ranging from 2.04 to 2.44 eV in the spin-down channel, they can be used for visible light photovoltaic devices, photodetectors, etc.[65,66] Moreover, these 2D MOFs can be also assembled into heterojunctions with other 2D materials such as graphene and MoS_2 to integrate more functional properties, further expanding their applications.[9]

CONCLUSIONS

To summarize, on the basis of first-principles calculations, we report a class of unprecedented 2D multifunctional SCs with several unique properties including auxetic effect, room-temperature ferrimagnetism, chiral FE, electrically controllable spin polarization, and topological nodal lines/points. The simultaneous realization of these functions relies on the combined tuning of the spin state of organic linkers and the symmetry/TL of the lattice structure in MOFs constructed by Cr(II) and inversion symmetry-breaking five-membered aromatic heterocycles (TDZ, ODZ, and SDZ). These materials not only serve as promising candidates for studying different proximity effects and designing multifunctional nanodevices but also imply the unique abilities of MOFs in obtaining electronic/magnetic properties that are difficult to achieve in inorganic materials such as chiral vortex−antivortex polar states in the monolayer limit.

COMPUTATIONAL METHODS

DFT calculations are performed by using the projector-augmented wave method and the Perdew−Burke−Ernzerhof (PBE) functional as implemented in Vienna ab initio Simulation Package (VASP).[67,68] The approach of Grimme (DFT-D3) with Becke−Jonson damping is adopted for the $\pi-\pi$ type van der Waals (vdW) interactions between the neighboring organic rings around Cr atoms.[69] To treat the partially filled $3d$ orbitals of transition metal atoms, the strongly correlated correction is considered with the PBE + U method.[70] The values of effective exchange interaction parameter (J) and onsite Coulomb interaction parameter (U) are, respectively, set as 1.0 and 3.0 eV, which are the same as those of the previously calculated Cr(pyz)$_2$ sheet.[12,13] In addition, we also test the magnetic exchange energies under different U values, and find that when U = 3 eV, the calculated relative energies ΔE of the FM state to the FiM1 state for the Cr(TDZ)$_2$ sheet is closest when using the hybrid HSE06 functional (Table S8). The energy cutoff for the plane-wave basis set is 520 eV. For the first Brillouin zone integration, the Monkhorst−Pack k-point mesh is used with a grid spacing less than 0.02 Å^{-1}, corresponding to a k-mesh size of 6 × 6 × 1. The energy and force criteria for convergence are set to 1 × 10^{-6} eV and 0.01 eV/Å, respectively. A vacuum region of about 15 Å is chosen to avoid mirror interactions between periodic layers. All structural data involved in the main text are listed in Tables S9−S19. The phonon spectrum is simulated by using the finite displacement method as implemented in Phonopy package interfaced with VASP,[71] where the magnetic ordering and the exchange-correlation effect are also included. A 2 × 2 × 1 supercell with a Monkhorst−Pack k-point mesh of 2 × 2 × 1 is adopted. The thermal stability is assessed according to the AIMD simulation at 400 K by using a 2 × 2 × 1 supercell. The climbing image nudged elastic band method is adopted to investigate the structure of the transition state and the energy barrier between different ferroelectric phases.[72] Considering the complicated transition between different ferroelectric phases, a series of possible structures on the intermediate path are conjectured to find the structure with the highest energy, and their phonon spectra are further analyzed to verify that they are indeed saddle points (Figure S18).

The out-of-plane electric polarization is evaluated by using the dipole correction scheme.[35] To accurately calculate the electronic structure, the screened hybrid HSE06 functional is applied, which includes the accurate Hartree−Fock exchange, short-range PBE exchange, long-range PBE exchange, and PBE correlation terms,[73,74] and is widely considered to perform much better than the PBE and PBE + U methods without the need to incorporate additional on-site Coulomb repulsion and correlation effect.[75−77]

The Monte Carlo simulations are performed by using property analysis and simulation package for materials software package.[78] During the simulations, a supercell of the 24 × 24 × 1 grid is used to reduce the periodic constraints. The spins on all magnetic sites can flip randomly in the simulation steps. The average magnetic moment (M) per unit cell and specific heat C_v are taken after the system reaches the equilibrium (with at least 10^5 simulation steps) state at a given temperature. The edge states have been performed using the open-source code WANNIERTOOLS[79] based on the Wannier tight-binding model constructed using the WANNIER90 code.[80] The irreps of the electronic bands are computed by the program IR2TB on the electronic Hamiltonian of the tight-binding model.[81]

ASSOCIATED CONTENT

Ⓢ Supporting Information

The Supporting Information is available free of charge at https://pubs.acs.org/doi/10.1021/jacs.2c12780.

> Calculation formulae for energy level and occupation numbers, derivation of exchange parameters, two-band $k \cdot p$ Hamiltonian for SNLs and QNP and discussion of Cr$_n$(TDZ)$_m$, phonon spectra, AIMD simulation, mechanical property, energy levels of d and p orbitals, spin density of different magnetic states, electric polarization analysis, structures of the monolayer and bilayer, possible pathway for transition from S^1 to S^4 (S^3), and HSE + SOC band structure for Cr(TDZ)$_2$, Poisson's ratio, Curie temperature, HSE and HSE + SOC band structures for Cr(ODZ)$_2$ and Cr(SDZ)$_2$, electronic structures of Cr$_n$(TDZ)$_m$, summary of current 2D multifunctional materials, energies of different Cr-(TDZ)$_2$ phase structures, magnetic exchange parameters and ground state properties for Cr(TDZ)$_2$, Cr(ODZ)$_2$, and Cr(SDZ)$_2$, relative energies of the FM state to FiM1 state and electric polarization for Cr$_n$(TDZ)$_m$, and structural information for all 2D sheets (PDF)

AUTHOR INFORMATION

Corresponding Authors

Xingxing Li − *Hefei National Research Center for Physical Sciences at the Microscale and Department of Chemical Physics, University of Science and Technology of China, Hefei, Anhui 230026, China; Hefei National Laboratory, University of Science and Technology of China, Hefei 230088, China;* ⓘ orcid.org/0000-0001-7820-0772; Email: lixx@ustc.edu.cn

Jinlong Yang − *Hefei National Research Center for Physical Sciences at the Microscale and Department of Chemical Physics, University of Science and Technology of China, Hefei, Anhui 230026, China; Hefei National Laboratory, University of Science and Technology of China, Hefei 230088, China;* ⓘ orcid.org/0000-0002-5651-5340; Email: jlyang@ustc.edu.cn

Authors

Xiangyang Li − *Hefei National Research Center for Physical Sciences at the Microscale, University of Science and*

Technology of China, Hefei, Anhui 230026, China; School of Materials Science and Engineering, Anhui University, Hefei, Anhui 230601, China

Qing-Bo Liu − Hubei Key Laboratory of Optical Information and Pattern Recognition, Wuhan Institute of Technology, Wuhan 430073, China; School of Physics and Wuhan National High Magnetic Field Center, Huazhong University of Science and Technology, Wuhan 430074, China

Yongsen Tang − School of Science, Nanjing University of Posts and Telecommunications, Nanjing 210023, China

Wei Li − Department of Physics, University of Science and Technology of China, Hefei, Anhui 230026, China

Ning Ding − School of Physics, Southeast University, Nanjing 211189, China

Zhao Liu − Hefei National Research Center for Physical Sciences at the Microscale, University of Science and Technology of China, Hefei, Anhui 230026, China

Hua-Hua Fu − School of Physics and Wuhan National High Magnetic Field Center, Huazhong University of Science and Technology, Wuhan 430074, China; orcid.org/0000-0003-3920-6324

Shuai Dong − School of Physics, Southeast University, Nanjing 211189, China; orcid.org/0000-0002-6910-6319

Complete contact information is available at:
https://pubs.acs.org/10.1021/jacs.2c12780

Author Contributions

[¶]X.L., Q.-B.L., and Y.T. contributed equally to this work.

Notes

The authors declare no competing financial interest.

REFERENCES

(1) Lu, C.; Wu, M.; Lin, L.; Liu, J. M. Single-phase multiferroics: New materials, phenomena, and physics. *Natl. Sci. Rev.* **2019**, 6, 653−668.

(2) Zhang, H. Introduction: 2D materials chemistry. *Chem. Rev.* **2018**, 118, 6089−6090.

(3) Song, Q.; Occhialini, C. A.; Ergecen, E.; Ilyas, B.; Amoroso, D.; Barone, P.; Kapeghian, J.; Watanabe, K.; Taniguchi, T.; Botana, A. S.; Picozzi, S.; Gedik, N.; Comin, R. Evidence for a single-layer van der Waals multiferroic. *Nature* **2022**, 602, 601−605.

(4) Xu, M.; Huang, C.; Li, Y.; Liu, S.; Zhong, X.; Jena, P.; Kan, E.; Wang, Y. Electrical control of magnetic phase transition in a type-I multiferroic double-metal trihalide monolayer. *Phys. Rev. Lett.* **2020**, 124, No. 067602.

(5) Wu, D.; Lv, H.; Zhuo, Z.; Li, X.; Wu, X.; Yang, J. Orbital design of two-dimensional transition-metal peroxide kagome crystals with anionogenic dirac half-metallicity. *J. Phys. Chem. Lett.* **2021**, 12, 3528−3534.

(6) Song, B.; Zhou, Y.; Yang, H. M.; Liao, J. H.; Yang, L. M.; Yang, X. B.; Ganz, E. Two-dimensional anti-van't Hoff/Le Bel array AlB$_6$ with high stability, unique motif, triple dirac cones, and superconductivity. *J. Am. Chem. Soc.* **2019**, 141, 3630−3640.

(7) Wang, M.; Dong, R.; Feng, X. Two-dimensional conjugated metal-organic frameworks (2D c-MOFs): chemistry and function for MOFtronics. *Chem. Soc. Rev.* **2021**, 50, 2764−2793.

(8) Furukawa, H.; Cordova, K. E.; OKeeffe, M.; Yaghi, O. M. The chemistry and applications of metal-organic frameworks. *Science* **2013**, 341, No. 1230444.

(9) Xie, Z.; Zhang, B.; Ge, Y.; Zhu, Y.; Nie, G.; Song, Y.; Lim, C.-K.; Zhang, H.; Prasad, P. N. Chemistry, functionalization, and applications of recent monoelemental two-dimensional materials and their heterostructures. *Chem. Rev.* **2021**, 122, 1127−1207.

(10) Feng, Q.; Li, X.; Yang, J. Two-dimensional multifunctional metal-organic framework with intrinsic bipolar magnetic semiconductivity and negative Poissons ratio. *ACS Appl. Electron. Mater.* **2022**, 4, 3198−3204.

(11) Li, X.; Yang, J. Realizing two-dimensional magnetic semiconductors with enhanced Curie temperature by antiaromatic ring based organometallic frameworks. *J. Am. Chem. Soc.* **2019**, 141, 109−112.

(12) Li, X.; Lv, H.; Liu, X.; Jin, T.; Wu, X.; Li, X.; Yang, J. Two-dimensional bipolar magnetic semiconductors with high Curie-temperature and electrically controllable spin polarization realized in exfoliated Cr(pyrazine)$_2$ monolayers. *Sci. China Chem.* **2021**, 64, 2212−2217.

(13) Lv, H.; Li, X.; Wu, D.; Liu, Y.; Li, X.; Wu, X.; Yang, J. Enhanced Curie temperature of two-dimensional Cr(II) aromatic heterocyclic metal-organic framework magnets via strengthened orbital hybridization. *Nano Lett.* **2022**, 22, 1573−1579.

(14) Li, X.; Li, X.; Yang, J. Two-dimensional multifunctional metal-organic frameworks with simultaneous ferro−/ferrimagnetism and vertical ferroelectricity. *J. Phys. Chem. Lett.* **2020**, 11, 4193−4197.

(15) Li, X.; Yang, J. Toward room-temperature magnetic semiconductors in two-dimensional ferrimagnetic organometallic lattices. *J. Phys. Chem. Lett.* **2019**, 10, 2439−2444.

(16) Yang, Y.; Ji, J.; Feng, J.; Chen, S.; Bellaiche, L.; Xiang, H. Two-dimensional organic-inorganic room-temperature multiferroics. *J. Am. Chem. Soc.* **2022**, 144, 14907−14914.

(17) Peng, Y.; Li, Y.; Ban, Y.; Jin, H.; Jiao, W.; Liu, X.; Yang, W. Metal-organic framework nanosheets as building blocks for molecular sieving membranes. *Science* **2014**, 346, 1356−1359.

(18) Yan, L.; Silveira, O. J.; Alldritt, B.; Kezilebieke, S.; Foster, A. S.; Liljeroth, P. Two-dimensional metal-organic framework on superconducting NbSe$_2$. *ACS Nano* **2021**, 15, 17813−17819.

(19) Edema, J. J.; Gambarotta, S.; Meetsma, A.; Van Bolhuis, F.; Spek, A. L.; Smeets, W. J. The unpredictable structural features of chromium(II) pyrrolyls: synthesis and x-ray structures of monomeric square-planar (η^1-2,5-Me$_2$C$_4$H$_2$N)$_2$Cr(py)$_2$, square-pyramidal (η^1-2,5-C$_4$H$_4$N)$_2$Cr(py)$_3$, dimeric [(7-azaindolyl)$_2$Cr(DMF)]$_2$, and polymeric [(η^1-2,5-Me$_2$C$_4$N$_2$)$_4$CrNa$_2$(THF)$_2$(Et$_2$O)]$_n$. An aborted Cr-Cr quadruple bond formation? *Inorg. Chem.* **1990**, 29, 2147−2153.

(20) Forniés, J.; Martín, A.; Martín, L. F.; Menjón, B.; Zhen, H.; Bell, A.; Rhodes, L. F. The first structurally characterized homoleptic aryl-manganese(III) compound and the corresponding isoleptic and isoelectronic chromium(II) derivative. *Organometallics* **2005**, 24, 3266−3271.

(21) Perlepe, P.; Oyarzabal, I.; Mailman, A.; Yquel, M.; Platunov, M.; Dovgaliuk, I.; Rouzières, M.; Négrier, P.; Mondieig, D.; Suturina, E. A.; Dourges, M.-A.; Bonhommeau, S.; Musgrave, R. A.; Pedersen, K. S.; Chernyshov, D.; Wilhelm, F.; Rogalev, A.; Mathonière, C.;

Clérac, R. Metal-organic magnets with large coercivity and ordering temperatures up to 242°C. *Science* **2020**, *370*, 587−592.

(22) Das, S.; Tang, Y. L.; Hong, Z.; Goncalves, M. A. P.; McCarter, M. R.; Klewe, C.; Nguyen, K. X.; Gomez-Ortiz, F.; Shafer, P.; Arenholz, E.; Stoica, V. A.; Hsu, S.-L.; Wang, B.; Ophus, C.; Liu, J. F.; Nelson, C. T.; Saremi, S.; Prasad, B.; Mei, A. B.; Schlom, D. G.; Íñiguez, J.; García-ernández, P.; Muller, D. A.; Chen, L. Q.; Junquera, J.; Martin, L. W.; Ramesh, R. Observation of room-temperature polar skyrmions. *Nature* **2019**, *568*, 368−372.

(23) Yadav, A. K.; Nelson, C. T.; Hsu, S. L.; Hong, Z.; Clarkson, J. D.; Schlepu, T. C. M.; Damodaran, A. R.; Shafer, P.; Arenholz, E.; Dedon, L. R.; Chen, D.; Vishwanath, A.; Minor, A. M.; Chen, L. Q.; Scott, J. F.; Martin, L. W.; Ramesh, R. Observation of polar vortices in oxide superlattices. *Nature* **2016**, *530*, 198−201.

(24) Li, X.; Wu, X.; Li, Z.; Yang, J.; Hou, J. G. Bipolar magnetic semiconductors: A new class of spintronics materials. *Nanoscale* **2012**, *4*, 5680−5685.

(25) Li, X.; Wu, X.; Yang, J. Half-metallicity in $MnPSe_3$ exfoliated nanosheet with carrier doping. *J. Am. Chem. Soc.* **2014**, *136*, 11065−11069.

(26) Lu, J.; Chen, G.; Luo, W.; Íñiguez, J.; Bellaiche, L.; Xiang, H. Ferroelectricity with asymmetric hysteresis in metallic $LiOsO_3$ ultrathin films. *Phys. Rev. Lett.* **2019**, *122*, No. 227601.

(27) Bertolazzi, S.; Brivio, J.; Kis, A. Stretching and breaking of ultrathin MoS_2. *ACS Nano* **2011**, *5*, 9703−9709.

(28) Mousanezhad, D.; Haghpanah, B.; Ghosh, R.; Hamouda, A. M.; Nayeb-Hashemi, H.; Vaziri, A. Elastic properties of chiral, anti-chiral, and hierarchical honeycombs: A simple energy-based approach. *Theor. Appl. Mech. Lett.* **2016**, *6*, 81−96.

(29) Fan, D.; Li, M.; Qiu, J.; Xing, H.; Jiang, Z.; Tang, T. Novel method for preparing auxetic foam from closed-cell polymer foam based on the steam penetration and condensation process. *ACS Appl. Mater. Interfaces* **2018**, *10*, 22669−22677.

(30) Peng, R.; Ma, Y.; He, Z.; Huang, B.; Kou, L.; Dai, Y. Single-layer Ag_2S: A two-dimensional bidirectional auxetic semiconductor. *Nano Lett.* **2019**, *19*, 1227−1233.

(31) Wang, Y.; Li, F.; Li, Y.; Chen, Z. Semi-metallic Be_5C_2 monolayer global minimum with quasi-planar pentacoordinate carbons and negative Poisson's ratio. *Nat. Commun.* **2016**, *7*, 11488.

(32) Zhang, L.-C.; Qin, G.; Fang, W.-Z.; Cui, H.-J.; Zheng, Q.-R.; Yan, Q.-B.; Su, G. Tinselenidene: A two-dimensional auxetic material with ultralow lattice thermal conductivity and ultrahigh hole mobility. *Sci. Rep.* **2016**, *6*, 19830.

(33) Cai, K.; Luo, J.; Ling, Y.; Wan, J.; Qin, Q.-H. Effects of size and surface on the auxetic behaviour of monolayer graphene kirigami. *Sci. Rep.* **2016**, *6*, 35157.

(34) Xiang, H. J.; Wei, S.-H.; Whangbo, M.-H. Origin of the structural and magnetic anomalies of the layered compound $SrFeO_2$: A density functional investigation. *Phys. Rev. Lett.* **2008**, *100*, No. 167207.

(35) Ding, W.; Zhu, J.; Wang, Z.; Gao, Y.; Xiao, D.; Gu, Y.; Zhang, Z.; Zhu, W. Prediction of intrinsic two-dimensional ferroelectrics in In_2Se_3 and other III_2-VI_3 van der Waals materials. *Nat. Commun.* **2017**, *8*, 14956.

(36) Choi, T.; Horibe, Y.; Yi, H. T.; Choi, Y. J.; Wu, W.; Cheong, S. W. Insulating interlocked ferroelectric and structural antiphase domain walls in multiferroic $YMnO_3$. *Nat. Mater.* **2010**, *9*, 253−258.

(37) Yasuda, K.; Wang, X.; Watanabe, K.; Taniguchi, T.; Jarillo-Herrero, P. Stacking-engineered ferroelectricity in bilayer boron nitride. *Science* **2021**, *372*, 1458−1462.

(38) Wu, M.; Li, J. Sliding ferroelectricity in 2D van der Waals materials: Related physics and future opportunities. *Proc. Natl. Acad. Sci. U. S. A.* **2021**, *118*, No. e2115703118.

(39) Chandrasekaran, A.; Mishra, A.; Singh, A. K. Ferroelectricity, antiferroelectricity, and ultrathin 2D electron/hole gas in multifunctional monolayer MXene. *Nano Lett.* **2017**, *17*, 3290−3296.

(40) Lin, L.-F.; Zhang, Y.; Moreo, A.; Dagotto, E.; Dong, S. Frustrated dipole order induces noncollinear proper ferrielectricity in two dimensions. *Phys. Rev. Lett.* **2019**, *123*, No. 067601.

(41) Zhao, Y.; Lin, L.; Zhou, Q.; Li, Y.; Yuan, S.; Chen, Q.; Dong, S.; Wang, J. Surface vacancy-induced switchable electric polarization and enhanced ferromagnetism in monolayer metal trihalides. *Nano Lett.* **2018**, *18*, 2943−2949.

(42) Khomskii, D. Trend: Classifying multiferroics: Mechanisms and effects. *Physics* **2009**, *2*, 20.

(43) Zou, R.; Zhan, F.; Zheng, B.; Wu, X.; Fan, J.; Wang, R. Intrinsic quantum anomalous Hall phase induced by proximity in the van der Waals heterostructure germanene/$Cr_2Ge_2Te_6$. *Phys. Rev. B* **2020**, *101*, No. 161108.

(44) Li, S.; Yu, Z.-M.; Liu, Y.; Guan, S.; Wang, S.-S.; Zhang, X.; Yao, Y.; Yang, S. A. Type-II nodal loops: Theory and material realization. *Phys. Rev. B* **2017**, *96*, No. 081106.

(45) Son, D. T.; Spivak, B. Z. Chiral anomaly and classical negative magnetoresistance of Weyl metals. *Phys. Rev. B* **2013**, *88*, No. 104412.

(46) Cano, J.; Bradlyn, B.; Wang, Z.; Hirschberger, M.; Ong, N. P.; Bernevig, B. A. Chiral anomaly factory: Creating Weyl fermions with a magnetic field. *Phys. Rev. B* **2017**, *95*, No. 161306.

(47) de Juan, F.; Grushin, A. G.; Morimoto, T.; Moore, J. E. Quantized circular photogalvanic effect in Weyl semimetals. *Nat. Commun.* **2017**, *8*, 15995.

(48) Ji, Z.; Liu, G.; Addison, Z.; Liu, W.; Yu, P.; Gao, H.; Liu, Z.; Rappe, A. M.; Kane, C. L.; Mele, E. J.; Agarwal, R. Spatially dispersive circular photogalvanic effect in a Weyl semimetal. *Nat. Mater.* **2019**, *18*, 955−962.

(49) Bandyopadhyay, A.; Majumdar, A.; Chowdhury, S.; Ahuja, R.; Jana, D. 8-16-4 graphyne: Square-lattice two-dimensional nodal line semimetal with a nontrivial topological Zak index. *Phys. Rev. B* **2021**, *103*, No. 075137.

(50) Wang, Z. F.; Liu, Z.; Liu, F. Quantum anomalous Hall effect in 2D organic topological insulators. *Phys. Rev. Lett.* **2013**, *110*, No. 196801.

(51) Wang, A.; Zhang, X.; Feng, Y.; Zhao, M. Chern insulator and Chern half-metal states in the two-dimensional spin-gapless semiconductor $Mn_2C_6S_{12}$. *J. Phys. Chem. Lett.* **2017**, *8*, 3770−3775.

(52) Feng, Y.; Liu, N.; Gao, G. Spin transport properties in Dirac spin gapless semiconductors Cr_2X_3 with high Curie temperature and large magnetic anisotropic energy. *Appl. Phys. Lett.* **2021**, *118*, 112407.

(53) Pedersen, K. S.; Perlepe, P.; Aubrey, M. L.; Woodruff, D. N.; Reyes-Lillo, S. E.; Reinholdt, A.; Voigt, L.; Li, Z.; Borup, K.; Rouzieres, M.; Samohvalov, D.; Wilhelm, F.; Rogalev, A.; Neaton, J. B.; Long, J. R.; Clerac, R. Formation of the layered conductive magnet $CrCl_2(pyrazine)_2$ through redox-active coordination chemistry. *Nat. Chem.* **2018**, *10*, 1056−1061.

(54) Abdurakhmanova, N.; Floris, A.; Tseng, T. C.; Comisso, A.; Stepanow, S.; De Vita, A.; Kern, K. Stereoselectivity and electrostatics in charge-transfer Mn- and Cs-$TCNQ_4$ networks on Ag(100). *Nat. Commun.* **2012**, *3*, 940.

(55) Liu, B.; Miao, G.; Zhong, W.; Huang, X.; Su, N.; Guo, J.; Wang, W. Manipulating the electronic and magnetic properties of coordinated nickel atoms in metal-organic frameworks by hydrogenation. *ACS Nano* **2022**, *16*, 2147−2153.

(56) Stepanow, S.; Ohmann, R.; Leroy, F.; Lin, N.; Strunskus, T.; Woll, C.; Kern, K. Rational design of two-dimensional nanoscale networks by electrostatic interactions at surfaces. *ACS Nano* **2010**, *4*, 1813−1820.

(57) Burtch, N. C.; Heinen, J.; Bennett, T. D.; Dubbeldam, D.; Allendorf, M. D. Mechanical properties in metal-organic frameworks: emerging opportunities and challenges for device functionality and technological applications. *Adv. Mater.* **2018**, *30*, No. 1704124.

(58) Tan, J.-C.; Civalleri, B.; Lin, C.-C.; Valenzano, L.; Galvelis, R.; Chen, P.-F.; Bennett, T. D.; Mellot-Draznieks, C.; Zicovich-Wilson, C. M.; Cheetham, A. K. Exceptionally low shear modulus in a prototypical imidazole-based metal-organic framework. *Phys. Rev. Lett.* **2012**, *108*, No. 095502.

(59) Manriquez, J. M.; Yee, G. T.; McLean, R. S.; Epstein, A. J.; Miller, J. S. A room-temperature molecular/organic-based magnet. *Science* **1991**, *252*, 1415−1417.

(60) Miao, L.-P.; Ding, N.; Wang, N.; Shi, C.; Ye, H.-Y.; Li, L.; Yao, Y.-F.; Dong, S.; Zhang, Y. Direct observation of geometric and sliding ferroelectricity in an amphidynamic crystal. *Nat. Mater.* **2022**, *21*, 1158−1164.

(61) Tedrow, P. M.; Meservey, R. Spin-dependent tunneling into ferromagnetic nickel. *Phys. Rev. Lett.* **1971**, *26*, 192.

(62) Tedrow, P. M.; Meservey, R. Spin polarization of electrons tunneling from films of Fe, Co, Ni, and Gd. *Phys. Rev. B* **1973**, *7*, 318−326.

(63) Bao, S.; Wang, J.; Wang, W.; Cai, Z.; Li, S.; Ma, Z.; Wang, D.; Ran, K.; Dong, Z.-Y.; Abernathy, D.; Yu, S. L.; Wan, X.; Li, J. X.; Wen, J. Discovery of coexisting Dirac and triply degenerate magnons in a three-dimensional antiferromagnet. *Nat. Commun.* **2018**, *9*, 2591.

(64) Sierra, J. F.; Fabian, J.; Kawakami, R. K.; Roche, S.; Valenzuela, S. O. Van der Waals heterostructures for spintronics and opto-spintronics. *Nat. Nanotechnol.* **2021**, *16*, 856−868.

(65) Ren, X.; Liao, G.; Li, Z.; Qiao, H.; Zhang, Y.; Yu, X.; Wang, B.; Tan, H.; Shi, L.; Qi, X.; Zhang, H. Two-dimensional MOF and COF nanosheets for next-generation optoelectronic applications. *Coord. Chem. Rev.* **2021**, *435*, No. 213781.

(66) Agbo, P.; Nwofe, P. Structural and optical properties of sulphurised Ag_2S thin films. *Int. J. Thin Fil. Sci. Tec.* **2015**, *4*, 9−12.

(67) Perdew, J. P.; Burke, K.; Ernzerhof, M. Generalized gradient approximation made simple. *Phys. Rev. Lett.* **1996**, *77*, 3865.

(68) Kresse, G.; Furthmüller, J. Efficient iterative schemes for ab initio total-energy calculations using a plane-wave basis set. *Phys. Rev. B* **1996**, *54*, 11169.

(69) Johnson, E. R.; Becke, A. D. A post-Hartree-Fock model of intermolecular interactions: Inclusion of higher-order corrections. *J. Chem. Phys.* **2006**, *124*, 174104.

(70) Liechtenstein, A. I.; Anisimov, V. I.; Zaanen, J. Density-functional theory and strong interactions: Orbital ordering in Mott-Hubbard insulators. *Phys. Rev. B* **1995**, *52*, R5467−R5470.

(71) Parlinski, K.; Li, Z. Q.; Kawazoe, Y. First-principles determination of the soft mode in cubic ZrO_2. *Phys. Rev. Lett.* **1997**, *78*, 4063−4066.

(72) Henkelman, G.; Uberuaga, B. P.; Jonsson, H. A climbing image nudged elastic band method for finding saddle points and minimum energy paths. *J. Chem. Phys.* **2000**, *113*, 9901.

(73) Heyd, J.; Scuseria, G. E.; Ernzerhof, M. Hybrid functionals based on a screened Coulomb potential. *J. Chem. Phys.* **2003**, *118*, 8207−8215.

(74) Paier, J.; Marsman, M.; Hummer, K.; Kresse, G.; Gerber, I. C.; Ángyán, J. G. Screened hybrid density functionals applied to solids. *J. Chem. Phys.* **2006**, *124*, 154709.

(75) Marsman, M.; Paier, J.; Stroppa, A.; Kresse, G. Hybrid functionals applied to extended systems. *J. Phys. Condens. Matter* **2008**, *20*, No. 064201.

(76) Da Silva, J. L. F.; Ganduglia-Pirovano, M. V.; Sauer, J.; Bayer, V.; Kresse, G. Hybrid functionals applied to rare-earth oxides: The example of ceria. *Phys. Rev. B* **2007**, *75*, No. 045121.

(77) Wen, X.-D.; Martin, R. L.; Roy, L. E.; Scuseria, G. E.; Rudin, S. P.; Batista, E. R.; McCleskey, T. M.; Scott, B. L.; Bauer, E.; Joyce, J. J.; Durakiewicz, T. Effect of spin-orbit coupling on the actinide dioxides AnO_2 (An= Th, Pa, U, Np, Pu, and Am): A screened hybrid density functional study. *J. Chem. Phys.* **2012**, *137*, 154707.

(78) Lou, F.; Li, X. Y.; Ji, J. Y.; Yu, H. Y.; Feng, J. S.; Gong, X. G.; Xiang, H. J. PASP: Property analysis and simulation package for materials. *J. Chem. Phys.* **2021**, *154*, 114103.

(79) Wu, Q.; Zhang, S.; Song, H.-F.; Troyer, M.; Soluyanov, A. A. WannierTools: An open-source software package for novel topological materials. *Comput. Phys. Commun.* **2018**, *224*, 405−416.

(80) Mostofi, A. A.; Yates, J. R.; Pizzi, G.; Lee, Y.-S.; Souza, I.; Vanderbilt, D.; Marzari, N. An updated version of wannier90: A tool for obtaining maximally-localised Wannier functions. *Comput. Phys. Commun.* **2014**, *185*, 2309−2310.

(81) Gao, J.; Wu, Q.; Persson, C.; Wang, Z. Irvsp: To obtain irreducible representations of electronic states in the VASP. *Comput. Phys. Commun.* **2021**, *261*, No. 107760.

📖 Recommended by ACS

Broad Electronic Modulation of Two-Dimensional Metal–Organic Frameworks over Four Distinct Redox States

Lei Wang, John S. Anderson, *et al.*

APRIL 05, 2023
JOURNAL OF THE AMERICAN CHEMICAL SOCIETY   READ 🔗

Ligand-Mediated Hydrogenic Defects in Two-Dimensional Electrically Conductive Metal–Organic Frameworks

Tekalign T. Debela, Christopher H. Hendon, *et al.*

MAY 04, 2023
JOURNAL OF THE AMERICAN CHEMICAL SOCIETY   READ 🔗

Conjugated Nonplanar Copper-Catecholate Conductive Metal–Organic Frameworks via Contorted Hexabenzocoronene Ligands for Electrical Conduction

Guolong Xing, Long Chen, *et al.*

APRIL 17, 2023
JOURNAL OF THE AMERICAN CHEMICAL SOCIETY   READ 🔗

Reticular Chemistry with Art: A Case Study of Olympic Rings-Inspired Metal–Organic Frameworks

Jincheng Si, Jing Li, *et al.*

NOVEMBER 23, 2022
JOURNAL OF THE AMERICAN CHEMICAL SOCIETY   READ 🔗

Get More Suggestions >